Whirlwinds and Hairpins in the Atmospheric Surface Layer

STEVEN P. ONCLEY, OSCAR HARTOGENSIS,[a] AND CHENNING TONG[b]

Earth Observing Laboratory, National Center for Atmospheric Research,[c] Boulder, Colorado

(Manuscript received 11 December 2015, in final form 31 August 2016)

ABSTRACT

Vortices in the atmospheric surface layer are characterized using observations at unprecedented resolution from a fixed array of 31 turbulence sensors. During the day, these vortices likely are dust devils, though no visual observations are available for confirmation. At night, hairpin vortices appear to have been observed. The structure and dynamics of several types of vortices are described and related to other vortex investigations, including tornadoes and hurricanes.

1. Background

The existence of dust devils was noted more than 100 years ago (e.g., Danes 1901) and the term "whirlwind" appears over 20 times in the Bible (e.g., Ezekiel 1:4, King James Version). Current interest in dust-devil behavior is driven by the need to understand both their role in Earth's global aerosol budget (Koch and Renno 2005) and their influence on the geology and atmosphere of Mars (e.g., Balme et al. 2003). In the 1960s, Peter Sinclair developed instrumented mobile platforms to chase dust devils; from these measurements he obtained the general behavior of wind, temperature, and pressure within dust devils (Sinclair 1964, 1969). Fitzjarrald (1973) sampled dust devils in a similar manner, including measurements of the vertical velocity and vorticity. Forty years later, others were still carrying out these types of measurements, albeit with better sensors. For example, Tratt et al. (2003) drove a truck instrumented with ultrasonic anemometers, thermocouples, and a differential barometer through several dust devils in Arizona to simulate how similar observations could be made on Mars. Nevertheless, each event is sampled along only one horizontal track using this approach.

Only one study has observed the two-dimensional structure of dust devils. Bluestein et al. (2004) showed several cases of horizontal cross sections of dust devils observed by a high-resolution radar and noted characteristics similar to those of tornadoes. They found cases of both one-cell vortices with a vorticity maxima in the center and two-cell vortices with an annular region kinematically inferred to contain updrafts near the region of maximum wind (RMW), as described by Smith and Leslie (1976). Also seen were devil pairs rotating around each other, subvortices at asymmetric locations [as also seen in tornadoes (Wurman 2002; Lee and Wurman 2005, hereafter LW)], and Rossby waves propagating azimuthally around the vortex center.

Other dust-devil measurements have concentrated on statistical inventories, such as Kurgansky et al. (2011), who relied primarily on visual observations of dust devils and related their occurrence to the ambient conditions. They confirmed a "rule of thumb" that near-surface wind speed must be below $8\,\mathrm{m\,s^{-1}}$ for dust devils to occur and that the Obukhov length be in the range $0 < -L < \sim 20$–$30\,\mathrm{m}$.

All of these studies treat dust devils as a unique vortex classification. The AMS *Glossary of Meteorology* (Glickman 2000) defines one as "a small but vigorous whirlwind, usually of short duration, rendered visible by dust, sand, and debris picked up from the ground" and further describes it as having a typical diameter of 3–30 m, either cyclonic or anticyclonic rotation, mostly upward vertical velocity, possibly having secondary vortices, and "best developed" with a steep lapse rate in temperature close to the surface (over land).

[a] Current affiliation: Wageningen University, Wageningen, Netherlands.

[b] Current affiliation: Department of Mechanical Engineering, Clemson University, Clemson, South Carolina.

[c] The National Center for Atmospheric Research is sponsored by the National Science Foundation.

Corresponding author e-mail: Steven P. Oncley, oncley@ucar.edu

DOI: 10.1175/JAS-D-15-0368.1

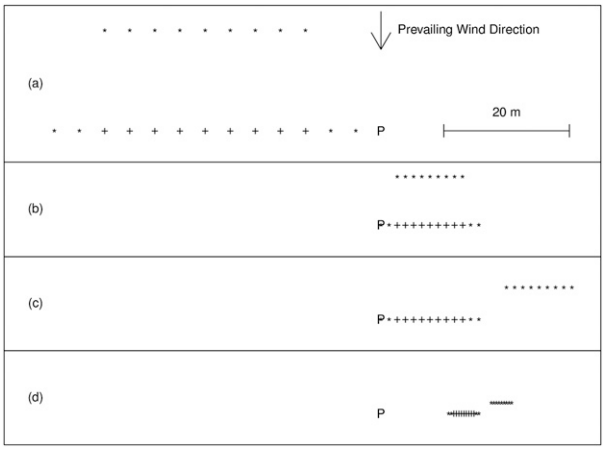

FIG. 1. Schematic layout of towers during the four AHATS configurations: (a) wide (4-m spacing), (b) medium (1.3-m spacing), (c) medium staggered, and (d) narrow staggered (0.4-m spacing). The bottom rake sensors were at heights of 3.24, 3.64, 4.83, and 6.98 m, respectively, and the top rake 1 m above the bottom rake. The profiler tower "P" was never moved. Locations with both top and bottom rake sensors are shown by plus signs.

This paper will show vortices that have only some of the above characteristics of dust devils. Indeed, we were forced to think beyond dust devils simply because our dataset contains no visual observations to confirm or deny that dust was present. Only once was a field log entry made that a dust devil was in the area. Furthermore, experienced observers were on site during at least one of the events shown below and did not comment on it in the field log.

2. Experiment

The measurements made during this study were part of the Advection Horizontal Array Turbulence Study (AHATS), which is the latest in a series of experiments to understand the interaction of turbulence statistics between spatial scales resolvable and those not resolved [e.g., by large-eddy simulations (LES)], based on the method of Tong et al. (1998). Other earlier experiments were the Horizontal Array Turbulence Study (HATS; Horst et al. 2004), the Ocean Horizontal Array Turbulence Study (OHATS; Kelly et al. 2009) over the ocean, and the Canopy Horizontal Array Turbulence Study (CHATS; Patton et al. 2011) in a walnut orchard. Nguyen et al. (2013) describe details of AHATS, so only a brief summary is included here. The field site was near Kettleman City, California, in a mowed, fallow, field chosen because it provided a flat and homogeneous fetch for at least 3 km and had a consistent wind direction. The vegetation was dry because of arid conditions. The soil is described by Arroues and Anderson (1986) as "Tulare clay" in the montmorillonitic group for which particle diameters on the order of 1 μm would be expected.

Thirty-one sonic anemometers were arranged in three parallel horizontal lines (rakes) and another six anemometers formed a vertical profile adjacent to these lines. The horizontal rakes consisted of a bottom rake containing 13 anemometers and 9 (later reduced to 8) pressure sensors, a top rake containing 9 anemometers and 5 pressure sensors, and a nominally upwind rake

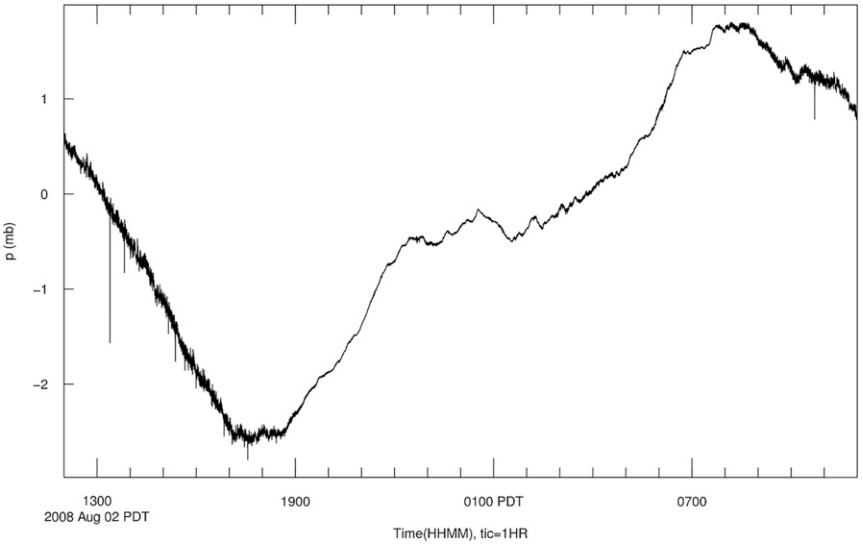

FIG. 2. Time series of pressure from the sensor at the center of the AHATS array for 24 h starting at 1200 PDT 2 Aug 2008. Note the negative spike at about 1300 PDT with a magnitude of approximately 1.5 mb (1 mb = 1 hPa) caused by a vortex event. Smaller magnitude spikes are seen at other times.

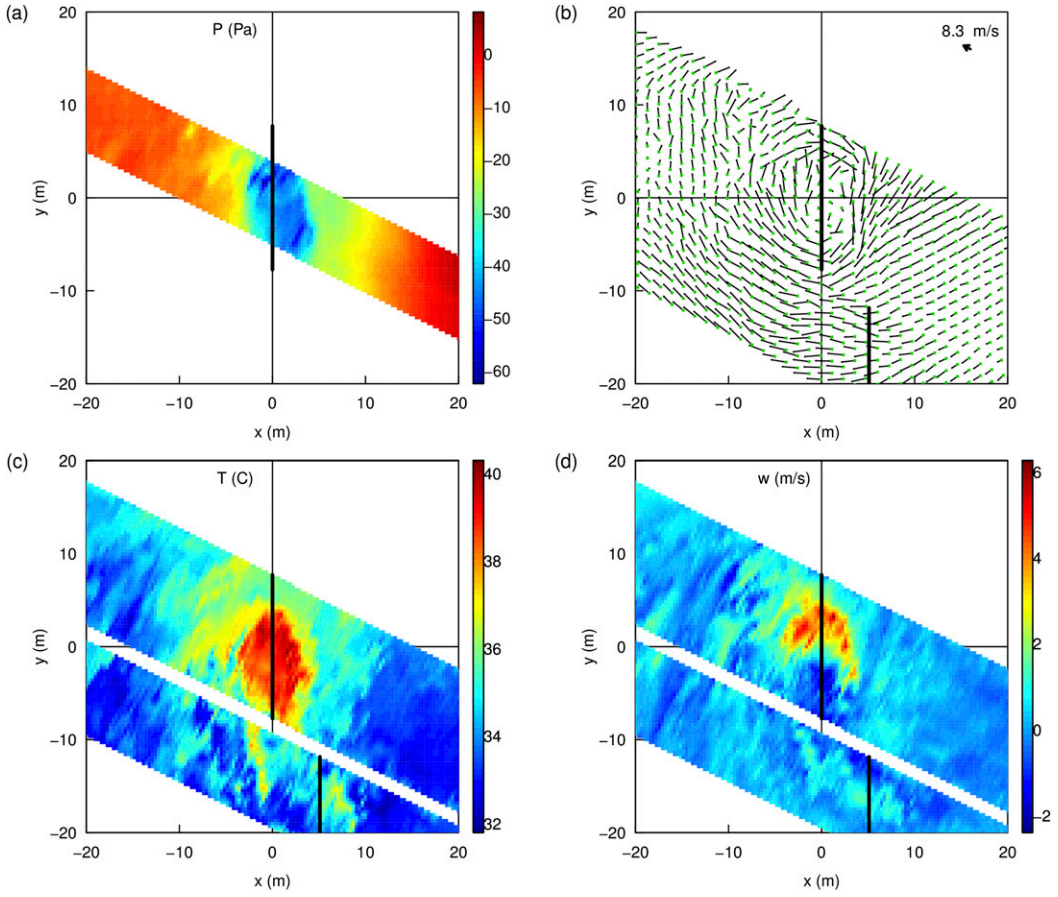

FIG. 3. A pseudohorizontal cross section of a whirlwind passing through the AHATS array at 1350 PDT 2 Aug 2008. (a) The pressure field (sampled only at the central 9 of 13 positions on the bottom rake), (b) the horizontal wind as vectors pointing in the wind direction from the sample location (green dots) with a length drawn to the same scale as the mean wind arrow, (c) the temperature field, and (d) the vertical velocity field. The measurements shown here, and in all but one of the following similar figures, are at $z = 4.83$ m. In (b)–(d), the position of the bottom rake is shown by the thick black line at $x = 0$ m and of the upwind rake is shown at $x \approx 5$ m. Time series from the sensors at these locations (subsampled to 10 samples per second) have been advected with the mean wind [shown as the arrow in the upper right in (b)].

with 9 anemometers. These were all oriented in the crosswind direction with respect to the predominate flow. Four combinations of heights and spacings of the anemometers along the horizontal lines were used during the study, which started 25 June and ended 16 August 2008 (Fig. 1). In the last two array configurations, the upwind rake was also displaced in the nominal crosswind direction to avoid contamination of the flow measured by the sensors farther downwind. Photographs of these arrays are published as online supplemental material in Nguyen et al. (2013).

As mentioned by Nguyen et al. (2013), the pressure measurements were made with differential pressure transducers all using the same reference pressure. For this study, we have not added this reference pressure to generate a true static pressure. Generally, the reference pressure signal contained low frequencies that are not relevant to the short-term events described here. It also was determined much later that the pressure transducer inlet filtered turbulence at frequencies above 1 Hz. This filtering does not significantly affect the results below.

3. Event identification

During AHATS, events that appeared to be (mostly negative) spikes were observed in the pressure signals (Fig. 2). Since these events were spatially and temporally coherent across the sensor array, they were not instrument artifacts. An hour-by-hour visual inspection of all the daytime data (over the 6 weeks of measurements) using just the central pressure sensor identified 136 pressure dips shorter than 1 min with an amplitude

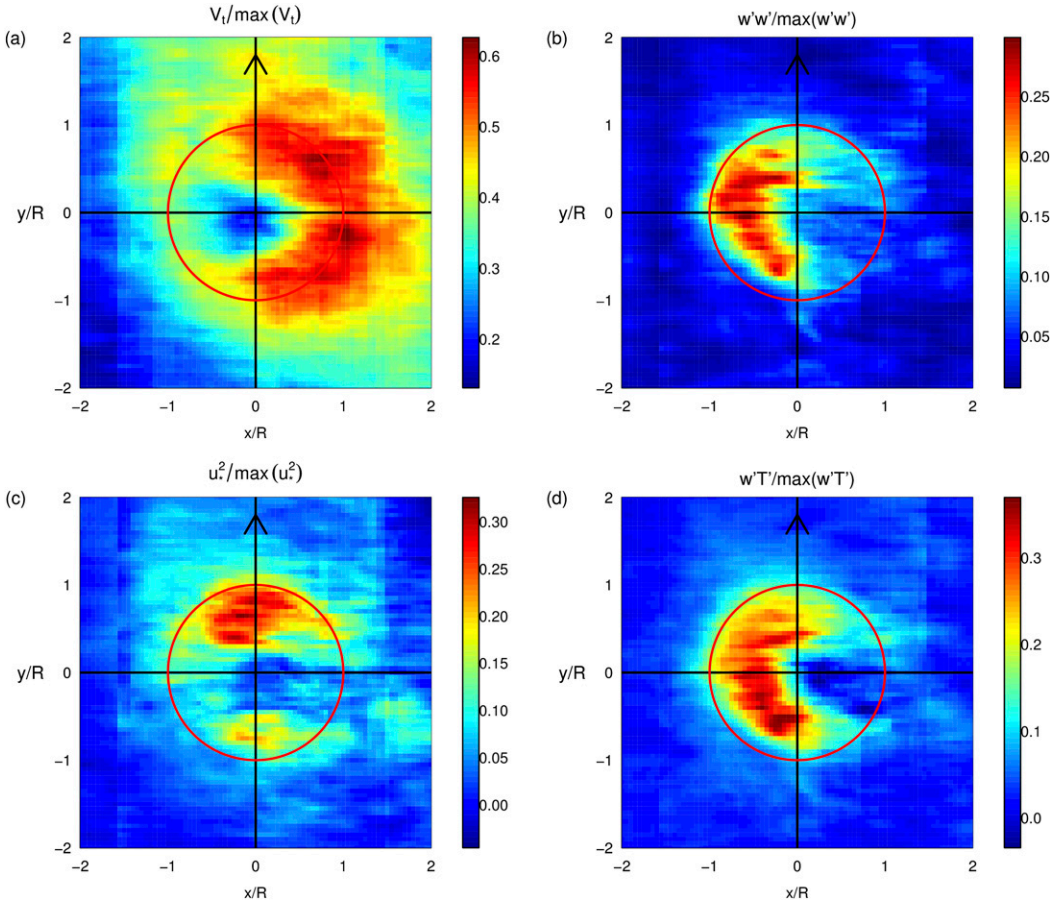

FIG. 4. A composite of horizontal slices of normalized (a) tangential velocity V_t, (b) vertical velocity variance w'^2, (c) momentum flux u_*^2, and (d) heat flux $w'T'$, for each of the 16 whirlwinds that were totally within the AHATS array. Each variable for each case was normalized before averaging by location to make the composite, so maximum values are less than 1.0. The arrow indicates the whirlwind propagation direction and a circle is shown with a normalized radius of 1. A subjective fit of a circle to each case was used to determine the center and radius, which, along with the mean wind direction and direction of rotation, were used to translate the position of each measurement to this figure.

of more than ~1.5 of the local standard deviation. Plotting the horizontal velocity in the manner of Fig. 3b showed that 70 (51%) of these dips were associated with horizontal rotation around an entire circle. Some of the other dips were associated with shear or convergence lines, but most defied classification.

We note that this number of cases—on average 2 day^{-1}—were sampled by a fixed array 10–50 m across. Indeed, this entire investigation was serendipitous, with the goal of AHATS being to study turbulence in a statistical manner and the site chosen simply to be representative of horizontally homogeneous flow. Thus, we conclude that vortices of this type are quite common for the conditions experienced. (A simple calculation using the advective wind speed, dimensions of the array, and the number and size of the events finds that they occupied 0.02% of the area in the afternoon, which is quite large.) However, as mentioned above, we have no information as to whether or not these vortices suspended particulate material. (We assume that dust is suspended only when the vertical velocity exceeds a threshold that depends on the surface and particulate characteristics.) Therefore, these whirlwinds might not have been visible for humans to notice.

To investigate the question posed by, for example, Kanak (2005) as to whether shear or heat flux drives these motions, we repeated this hour-by-hour event identification procedure for our nighttime data. Somewhat surprisingly, we found an additional 197 pressure events. The pressure dips for the vast majority of these nighttime cases were much smaller in magnitude than for the daytime cases but were detectable because of the

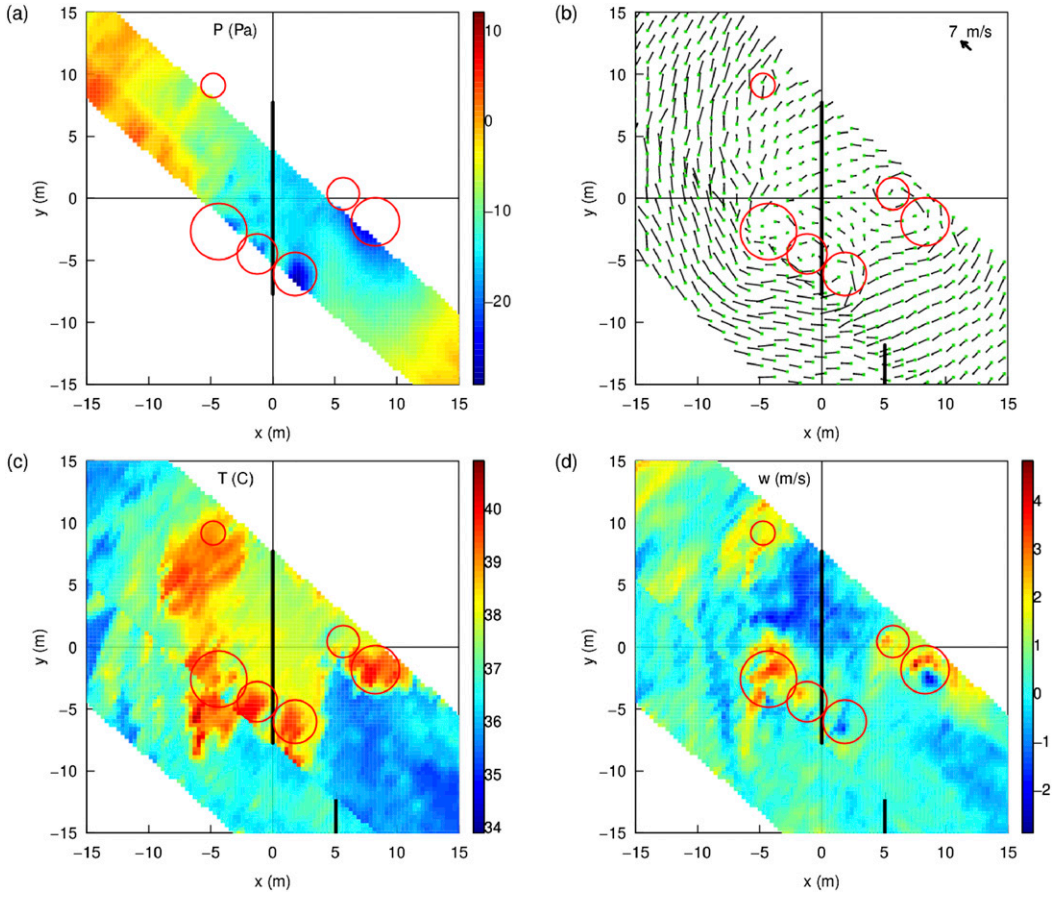

FIG. 5. As in Fig. 3, but for a whirlwind at 1540 PDT 2 Aug 2008. Note the multiple small vortices (indicated by red circles) embedded in the region of maximum tangential velocity.

generally lower turbulence levels (and thus pressure variance) at night. Few of the nighttime cases had the clear horizontal rotation seen during the day; however, 25% (discussed below) had identifiable rotation in some orientation.

4. Whirlwind characteristics

We find it useful to display the AHATS whirlwinds as pseudo–cross sections, using Taylor's hypothesis (Taylor 1938) in a manner similar to Fujita (1955) to transform our time series to distance in the direction of the mean wind. The mean wind was calculated from all of the anemometers in the bottom rake over a 2-min period, centered around the whirlwind. This mean wind also was subtracted from the horizontal velocity components. The period of 2 min was chosen to be short enough to represent the local conditions, but significantly longer than the period of the whirlwind events (typically less than 15 s) to avoid being dominated by the event itself. Clearly, the assumption of a "frozen field" is violated to an unknown extent for these events, so we expect that the resultant 2D "image" will be somewhat distorted from a true slice through the whirlwind. To expand the viewable domain, data from the upwind rake also are shown for the laterally offset array configurations. We can observe the breakdown of the frozen field assumption during these cases as a visual artifact caused by the small time difference of when the whirlwind was encountered by each rake. Nevertheless, this visualization appears to be a useful tool.

Figure 3 shows a good example of a whirlwind and is the smaller pressure spike [at 1350 Pacific daylight time (PDT)] in Fig. 2. This example contains several features that can be related to previous studies. First, the temperature field prior to the arrival (the left side of Fig. 3c) of the whirlwind ranges from 32° to 36°C. After the whirlwind passes, the temperature is much more uniform at about 32°C. This structure, in which air heated by the surface aggregates into a coherent structure and is replaced by more uniform, cooler air after the event passes, is similar to that of a convective plume (Kaimal

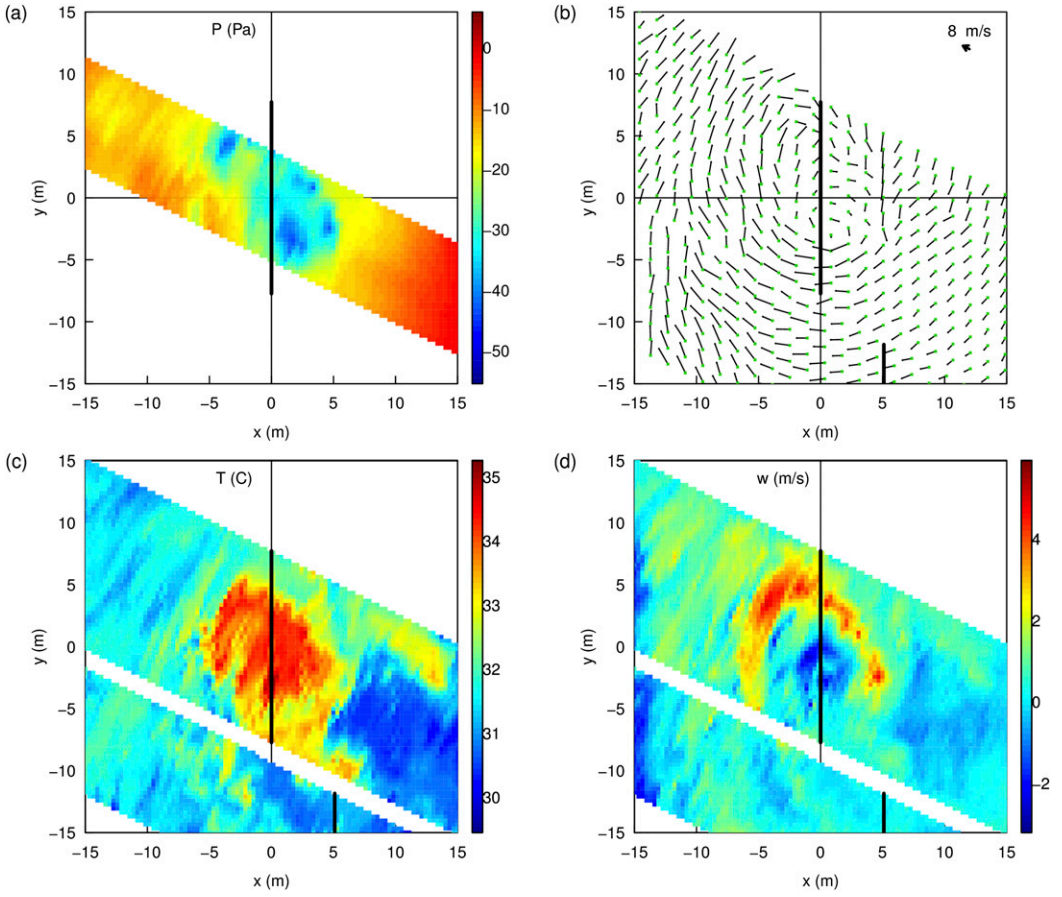

FIG. 6. As in Fig. 3, but for a whirlwind at 1042 PDT 3 Aug 2008. Note the concentric rings of alternating positive and negative vertical velocity.

and Businger 1970, hereafter KB; Wilczak and Tillman 1980; Garai et al. 2013). Vertical velocities from -2 to $+6\,\mathrm{m\,s^{-1}}$ are seen, similar to those observed by KB and Garai et al. (2013). However, the vertical velocities calculated by Gu et al. (2006) were much larger and those calculated by Raasch and Franke (2011, hereafter RF) are almost always positive (likely because of their lower spatial resolution).

The second characteristic is the apparent lack of azimuthal symmetry, especially in the vertical velocity. This asymmetry is seen in most, if not all, of the whirlwinds encountered during AHATS. A vertical tilt at an angle θ in an otherwise symmetric vortex would transform some of the horizontal velocity u in the direction of the tilt (i.e., u_t) into a vertical velocity $w = u_t \sin(\theta)$. Thus, an asymmetric pattern of updrafts on one side of the whirlwind and downdrafts on the other would be seen. This effect may be present in our data; however, the magnitude calculated for the tilt angles presented below is too small to explain magnitude of the observed asymmetry in w. For example, the case shown in Fig. 3 has $\theta = 3.3°$ and the maximum value of tangential velocity $V_t = 8.9\,\mathrm{m\,s^{-1}}$, which would produce an asymmetry in w of $\pm 0.5\,\mathrm{m\,s^{-1}}$. However, the maximum updrafts on either side of this vortex core are 6.2 and $1.5\,\mathrm{m\,s^{-1}}$—a difference that is more than 4 times the magnitude of the tilt effect. Model results presented by Gu et al. (2006) are generally symmetric, though they were produced without a mean wind. Models of vortices within a mean flow, such as Kepert and Wang (2001), show asymmetry in w (their Fig. 10) consistent with our observations.

Asymmetry in rotating geophysical flows has been observed in hurricanes. Shea and Gray (1973, hereafter SG) showed that the tangential (horizontal) wind speed had a maximum "to the right of track." Our dataset contains 16 cases in which the entire whirlwind was within our array that can be used to check for symmetry. With one exception, all of the cyclonic cases have a maximum in V_t to the right of track, as found by SG and others, and the anticyclonic cases to the left of track. (The exception is an anticyclonic case with local maxima

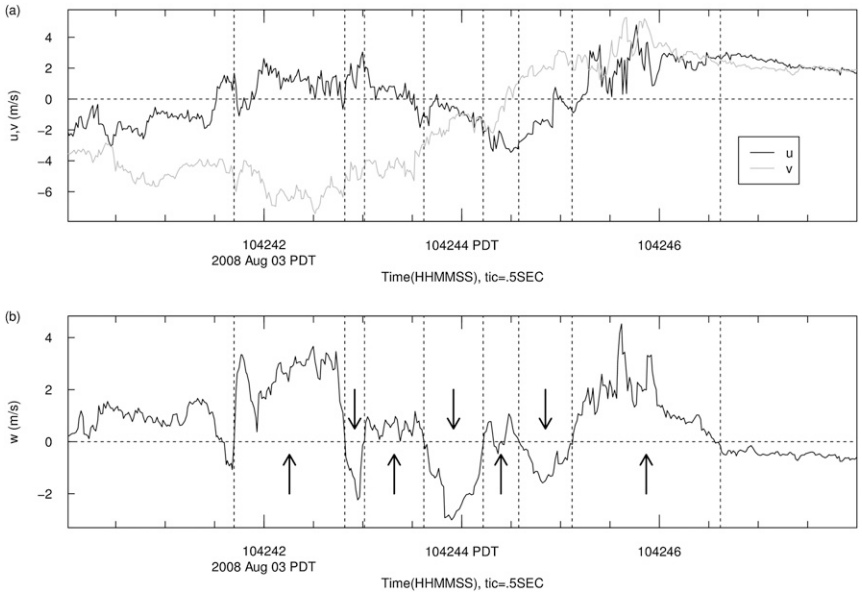

FIG. 7. The time series of (a) horizontal velocity components (u, v) and (b) vertical velocity w for the whirlwind shown in Fig. 6 as sampled by the anemometer closest to the center. A progression of updraft and downdraft regions is seen both before and after the center passes at 1042:44 PDT, mostly corresponding to the concentric (horizontal) rings.

on both sides.) We composited all of these cases after normalizing the data and positions and taking the mirror image ($y = -y$) when the rotation was anticyclonic. This composite (Fig. 4a) agrees remarkably well with SG's Fig. 20. Here, all cases were rescaled to radius-normalized horizontal coordinates using the center position and radius from a manual fit to the velocity and temperature data (described below) and the mean wind direction.

With our data, we also can compare our observations to those of KB, who show linear transects through the center of a dust devil of the three wind components, temperature, momentum flux, and sensible heat flux. Figures 4c and 4d show the spatial distribution of the vertical fluxes of momentum and sensible heat also composited over 16 cases. For these calculations, we have used the measured vertical velocity for w' and fluctuations of wind speed and temperature are with respect to the mean over the 2-min period centered around the whirlwind. The momentum flux calculation is for the residual scalar wind speed, to represent the total stress. Both fluxes agree quite well with KB's transect at a height of 22.6 m. Positive momentum fluxes are seen near both the leading and trailing edges, where the strongest winds occur in updrafts, and small negative fluxes in the center. Heat fluxes along the centerline of the whirlwind (as with KB's case) have a similar pattern with strong positive fluxes at the leading and trailing edges and a negative heat flux in the center. However, our data show that the strong flux region extends throughout the left of track part of the whirlwind. One interpretation of this behavior is that mechanical mixing in the high-velocity part of the whirlwind prevents strong heat fluxes from developing.

We now can revisit the question of whether these events are dust devils. Bagnold (1954) found that the saltation process of suspending particles followed Reynolds number scaling, using the friction velocity u_* as the scaling velocity. Following Iversen et al. (1976), we find that u_* must be greater than $1.7\,\mathrm{m\,s^{-1}}$ for saltation of the 1-μm cohesive particles at this site to occur and clumping of particles would reduce this u_* threshold. Although $u_* = 1.7\,\mathrm{m\,s^{-1}}$ is a large value, 7 of the above 16 cases exceed this threshold over more than half of the whirlwind area and 12 of the cases over at least a quarter of the area. One of the 16 cases exceeded this threshold over less than 3% of the area. Thus, it is likely that most of our whirlwinds were indeed dust devils.

Our second whirlwind example (Fig. 5) occurred less than 2 h after the case shown in Fig. 3. This whirlwind has multiple vortices embedded in the main rotation, as seen in the horizontal velocity and especially the temperature field. In this case, even the pressure field is distorted from the relatively symmetric dip seen in the event at 1350 PDT. This whirlwind is qualitatively similar to the 1999 Mullhall, Kansas, tornado documented by LW with multiple subtornadic-scale vortices. Each of the embedded vortices appear to rotate in the same

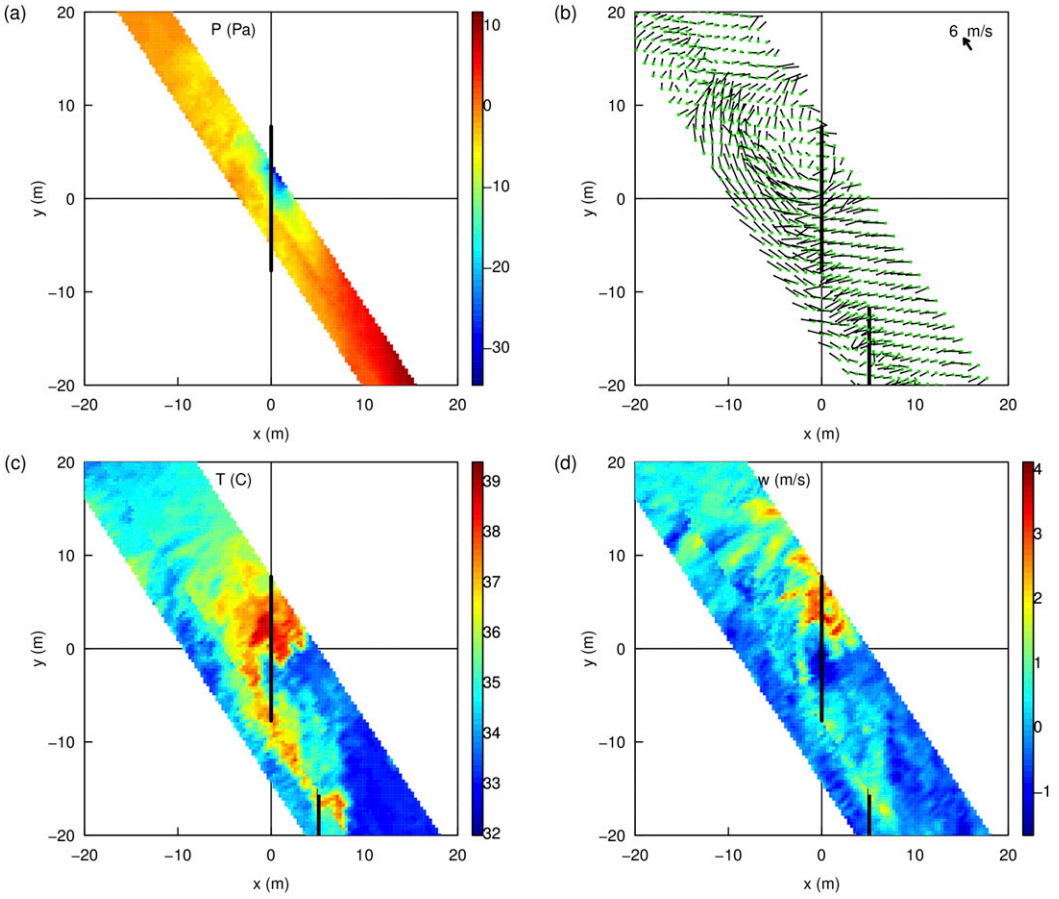

FIG. 8. As in Fig. 3, but for a whirlwind at 1318 PDT 1 Aug 2008. Note long "tail" in the $-y$ direction of warm temperature and, to a lesser extent, positive vertical velocity.

direction as the primary vortex (anticyclonic, here) and have updrafts in some portion, as speculated by LW. LW's embedded vortices were transient phenomena that occurred during the weakening phase of the tornado. Unfortunately, we cannot characterize the life stage of our whirlwind to confirm this timing. LW noted that embedded vortices can create local regions with significantly higher winds (and thus damage potential) than would be expected from the magnitude of the average tangential velocity. Although damage from whirlwinds rarely is an issue, any model of whirlwinds should include the potential for this characteristic.

We also see vortices that contain, when viewed as a horizontal cross section (Fig. 6), concentric rings of alternating positive and negative vertical velocity. Figure 7 shows the time series of the three velocity components (u, v, w) through the center of such a case on 1043 PDT 3 August 2008. This velocity pattern is identical to that of multicell structures of tornadoes described by Davies-Jones (1986). With (outward from the center) a downdraft–updraft–downdraft–updraft pattern, this case could be characterized as a four-cell vortex, with even an extra downdraft region in the leading edge. To our knowledge, this number of concentric cells has not been documented for tornadoes.

Kanak (2005) and RF have model results showing that vortices can develop at the intersections of convergence lines that are generated in cellular convection. These results are consistent with the description by Willis and Deardorff (1979) of plumes with "considerable vertical vorticity" generated in a laboratory flow by convergent horizontal flows at low levels, though they could not describe how this vorticity forms. RF describe a process in which velocity shear "generates horizontal vorticity, which is converted to vertical vorticity when the flow enters the updraft region of the vortex" and mention both hairpin vortices (see below) and formation of a particular convergence pattern as mechanisms for initial vorticity generation. We see a whirlwind at 1315 PDT 1 August 2008 (Fig. 8) that could be a convergence case. One convergence line extending for at least 10 whirlwind diameters upwind is seen as a line of

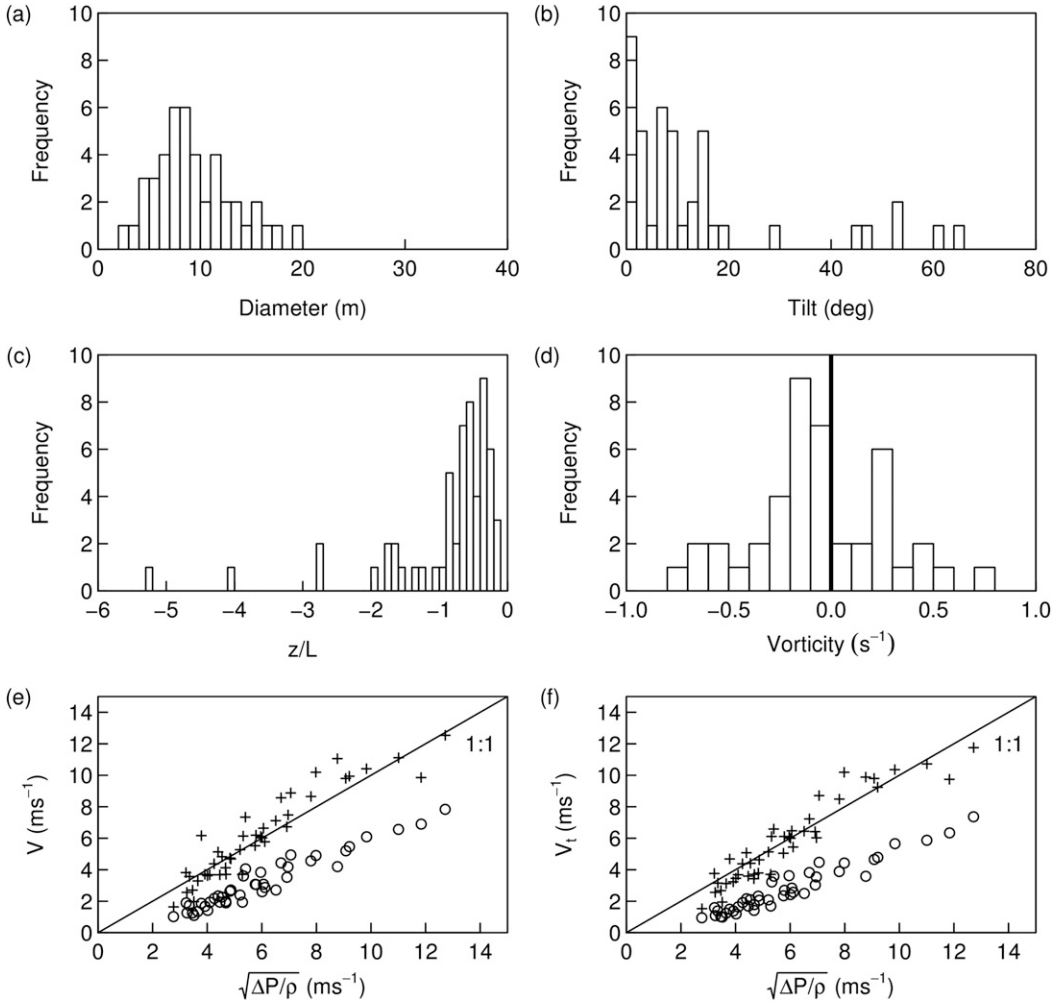

FIG. 9. Summary statistics for the daytime whirlwinds encountered during this study. (a) The distribution of sizes estimated manually using the horizontal and vertical wind, temperature, and pressure fields. (b) The distribution of tilt angles (from vertical) of the whirlwinds, estimated from the shift in the temperature field position measured by the top and bottom rakes. (c) The distribution of the stability parameter z/L. (d) The distribution of the vertical component of relative vorticity. (e) The average (circle) and maximum (plus signs) velocity vs the velocity derived from the pressure drop for all of the obvious AHATS whirlwinds. The velocities would be equal if the whirlwinds were in cyclostrophic balance. (f) As in (e), but for the average and maximum tangential component of the velocity.

positive vertical velocity and associated high temperatures (during daytime unstable conditions). Several other cases also had whirlwinds at the end of long convergence lines, though an intersection was not apparent. We also see 14 cases in which a whirlwind appears at the end of an offshoot of a kink in a convergence line. In other words, the horizontal cross section of the convergence line for these cases takes on the shape of the symbol λ, with a whirlwind at the top. Also all of the cases with close whirlwind pairs, including the nighttime case described below, appear to be on either side of a cross flow—a structure similar to vortices that ''rolled up'' at the edge of a thunderstorm outflow documented by Mueller and Carbone (1987). We cannot comment on the source of this cross flow.

With the large quantity of cases, we also can gather some statistics. For each of the 64 obvious whirlwinds, we fitted a circle by eye using the generally coincident criteria of maximum tangential velocity, continuity of curvature of the horizontal velocity field, maximum vertical velocity, and edge of the region of maximum temperature. As with all earlier studies (e.g., Carroll and Ryan 1970), there is no preferred direction of rotation, with 36 cases cyclonic and 28 cases anticyclonic. Figure 9 shows the distribution of daytime whirlwind sizes, stability parameter, and tilt angles encountered. The frequency of quite small sizes, with a peak diameter of 8 m, may have been a function of the array size and subjective detection method. The wind speed range (not shown)

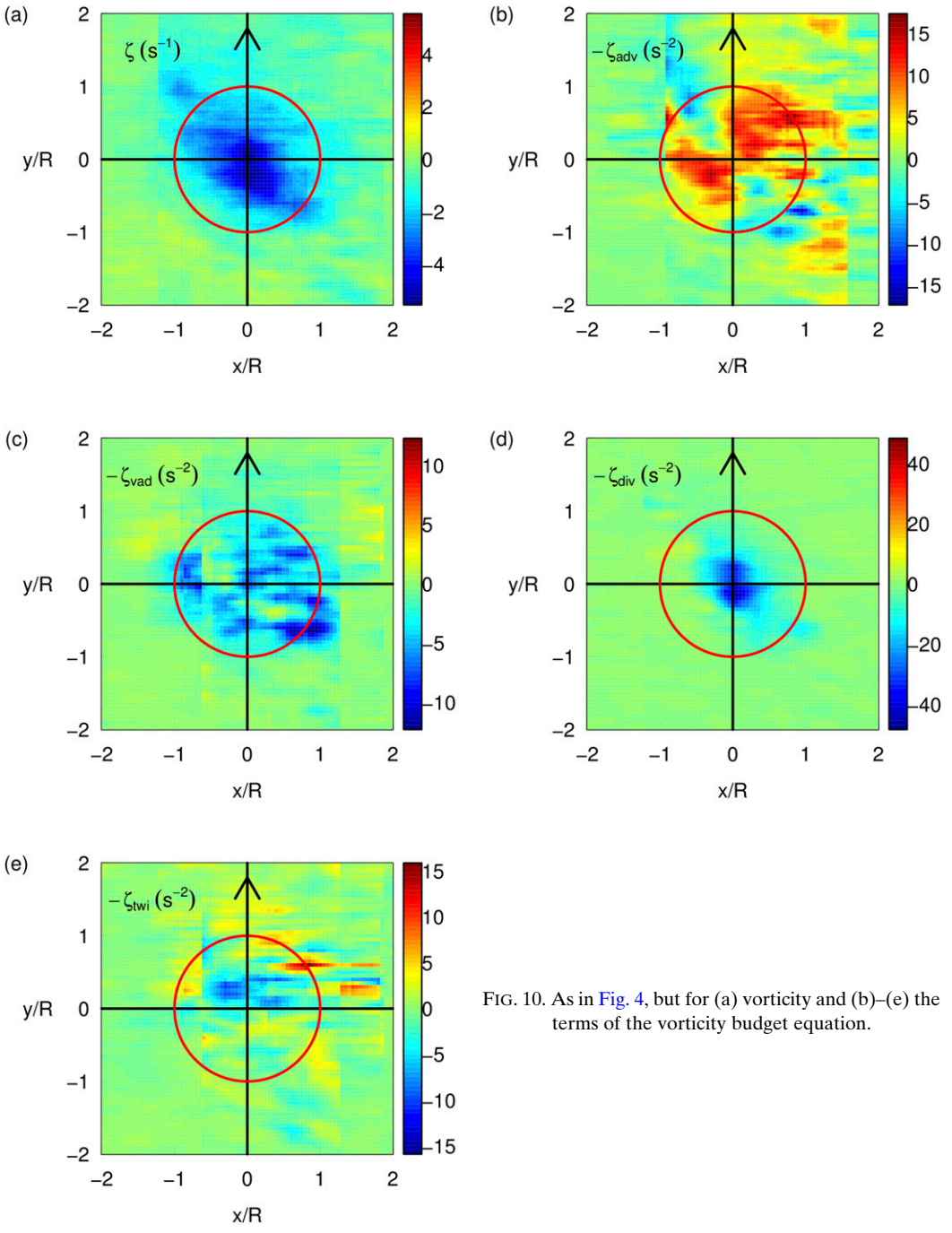

FIG. 10. As in Fig. 4, but for (a) vorticity and (b)–(e) the terms of the vorticity budget equation.

for all these cases is 1.0–4.5 m s^{-1}, which fits within the range encountered by Kurgansky et al. (2011). Our data cannot confirm the upper limit of 8 m s^{-1} that they found for whirlwinds to occur, since wind speeds during AHATS always were lower than this value. The stability range had only a few cases with $|-z/L| > 1$ (where z is the measurement height and L is the Obukhov length). These are conditions that commonly occur in many midlatitude land regions, suggesting that whirlwinds should exist beyond the hot and arid conditions where dust devils have been documented. The tilt angles, calculated by determining the spatial shift that maximizes the correlation of the temperature field measured by the top rake with that from the bottom rake, are mostly near vertical, though a few are significantly tilted across this 1-m vertical separation.

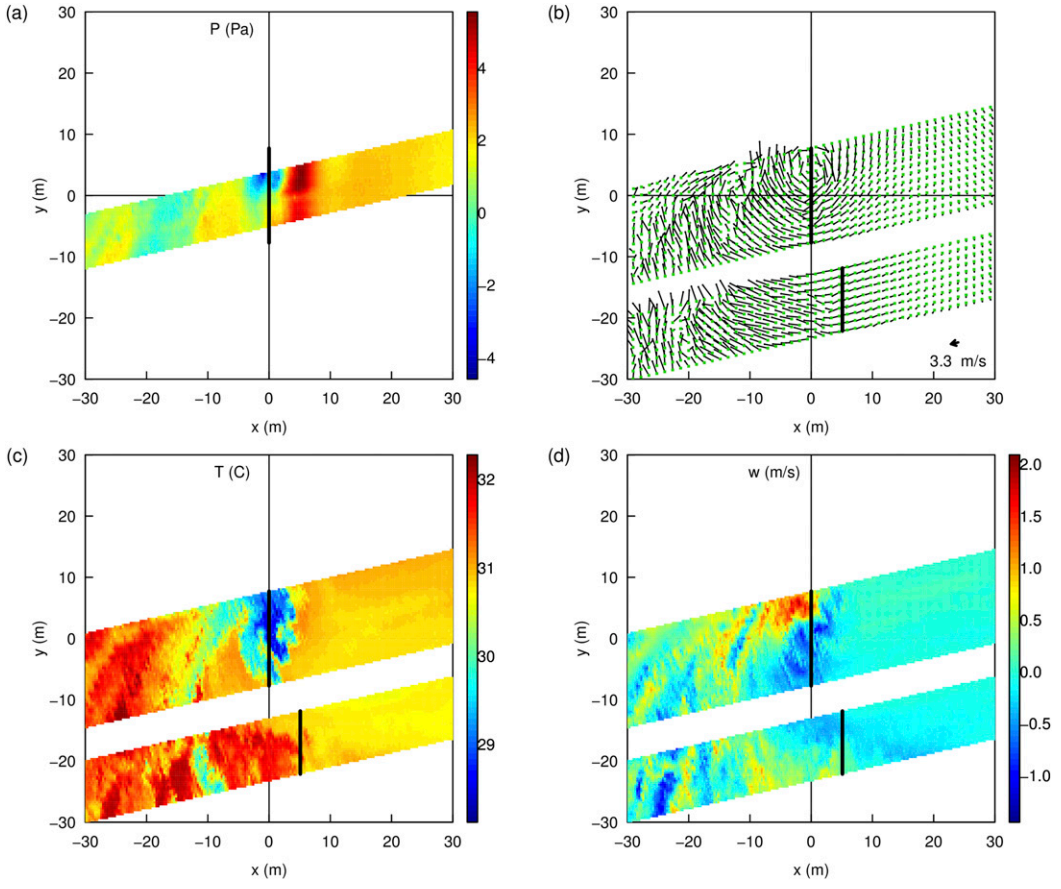

FIG. 11. As in Fig. 3, but for a whirlwind at 2211 PDT 4 Aug 2008. Noteworthy about this case is that it occurs well after sunset in stable conditions and thus has a cold core.

We also have computed the vertical component of vorticity ζ for these cases (Fig. 9d). Values were computed both from the direct calculation of $\partial v/\partial x - \partial u/\partial y$ averaged within the fitted circle and from the circulation $\mathbf{u} \cdot \mathbf{l}$ around the circle divided by the area, where $\mathbf{u}$ is the velocity vector and $\mathbf{l}$ is the unit vector around the circumference of the circle. Values using these two methods were similar, so the average of both methods was used. These values are similar in magnitude to the values between 0.5 and 1.0 s^{-1} found by Bluestein et al. (2004) for dust whirlwinds and for values typical of tornadoes (e.g., maximum of 0.35 s^{-1} found by LW).

Following RF and removing the small Coriolis and baroclinicity terms, the budget equation for ζ becomes

$$\frac{\partial \zeta}{\partial t} = -\zeta_{\text{adv}} - \zeta_{\text{vad}} - \zeta_{\text{div}} - \zeta_{\text{twi}}, \qquad (1)$$

in which the change of ζ with time t is the sum of terms representing horizontal advection ζ_{adv}, vertical advection ζ_{vad}, divergence ζ_{div}, and twisting ζ_{twi}, where

$$\zeta_{\text{adv}} = u\frac{\partial \zeta}{\partial x} + v\frac{\partial \zeta}{\partial y},$$

$$\zeta_{\text{vad}} = w\frac{\partial \zeta}{\partial z},$$

$$\zeta_{\text{div}} = \zeta\left(\frac{\partial u}{\partial x} + \frac{\partial v}{\partial y}\right), \quad \text{and}$$

$$\zeta_{\text{twi}} = \frac{\partial w}{\partial x}\frac{\partial v}{\partial z} + \frac{\partial w}{\partial y}\frac{\partial u}{\partial z}.$$

We can compute all of these terms, with the exception of the time derivative, over some portion of the array. A composite over 16 vortices of all these terms, in the same manner as for Fig. 4 above, is shown in Fig. 10. Gradients in the x direction were computed from samples 0.6 s apart to more closely match the spatial separation in the y direction. There is a tendency for ζ to be larger in quadrants II and IV, which is consistent with ζ_{adv} being positive in quadrants I and III. The values of vorticity near the vortex core of approximately $-4\,s^{-1}$ are in excellent agreement with RF and, similar to RF, the largest terms are ζ_{adv} and ζ_{div} with the largest values for

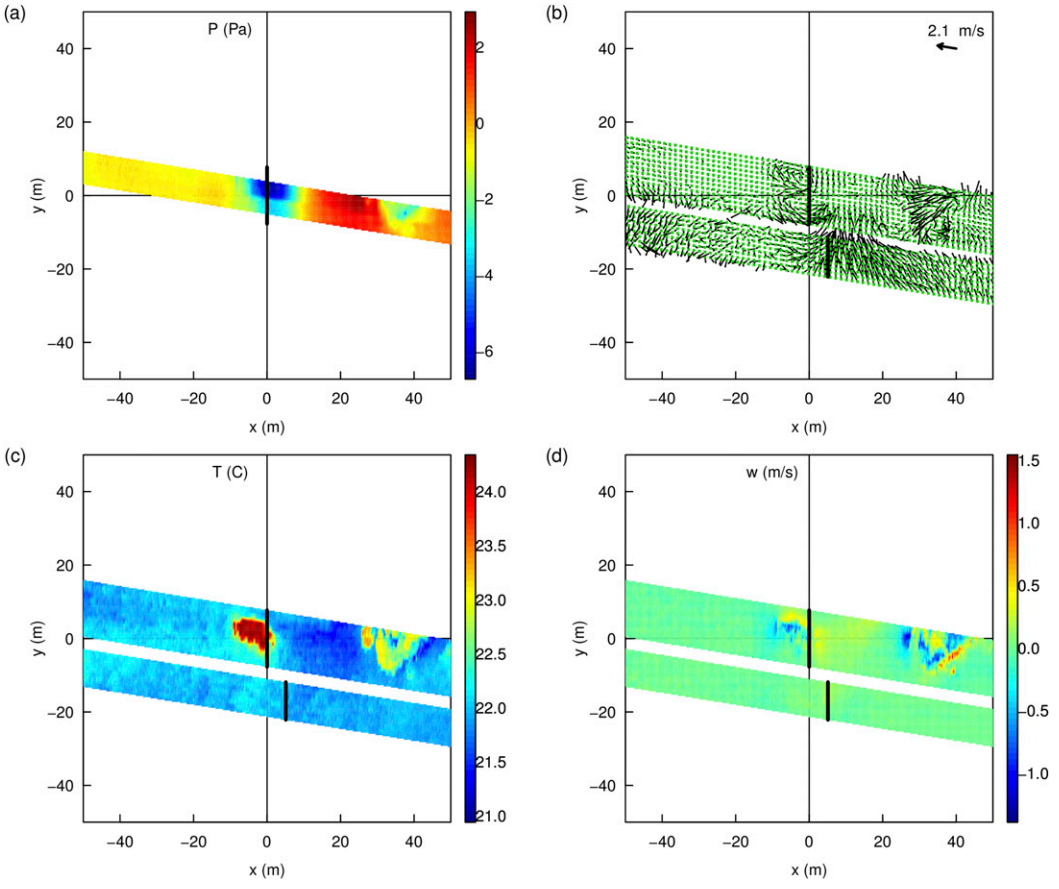

FIG. 12. As in Fig. 3, but for a pair of night whirlwinds at 0429 PDT 5 Aug 2008. Note the vertical velocity asymmetry for both cases.

ζ_{div} located near the vortex center. Unlike RF, our values for these terms are at least two orders of magnitude larger than those given for their vortex *A*. RF point out that their values are ''at the lower limit'' of those from observations, primarily because of (still) insufficient LES grid resolution, which could cause the gradients to be underestimated. Indeed, we often observe wind speed differences of several meters per second between adjacent instruments—even with an array spacing of only 0.4 m.

We calculate the cyclostrophic balance of these whirlwinds using the total (Fig. 9e) and tangential velocity (Fig. 9f). In both plots, the calculation is shown using both the average and maximum velocity $v_{\max}$ around the fitted circle. In a friction-free fluid, cyclostrophic balance is expected, which clearly is not the case for the average tangential velocity. The maximum total velocities $v_{\max}$ often appear to be somewhat supercyclostrophic. This behavior has been noted by many authors for larger vortices and Kepert and Wang (2001), for example, have modeled supergradient winds in terms of the dynamics of the flow. A contributing factor also could be the presence of the small embedded vortices described above, for which the portion moving in the mean rotation direction would have a velocity higher than the average. If true, the number of these cases suggests that embedded vortices are quite common; however, they were observed in only 9 of the 70 daytime cases. The tendency for supercyclostrophic behavior is less obvious using the tangential velocity; thus, a radial flow component (divergence, convergence, or embedded vortices) apparently contributes to this behavior. It also is possible that low-pass filtering, with a cutoff frequency estimated at about 1 Hz, by the pressure transducer internal tubing, systematically underestimated the amplitude of the pressure change ΔP, calculated as the median minus the minimum pressure for ± 1 min from each case.

5. Night cases

As mentioned above, about 200 pressure dips were found in the nighttime data. Although sometimes

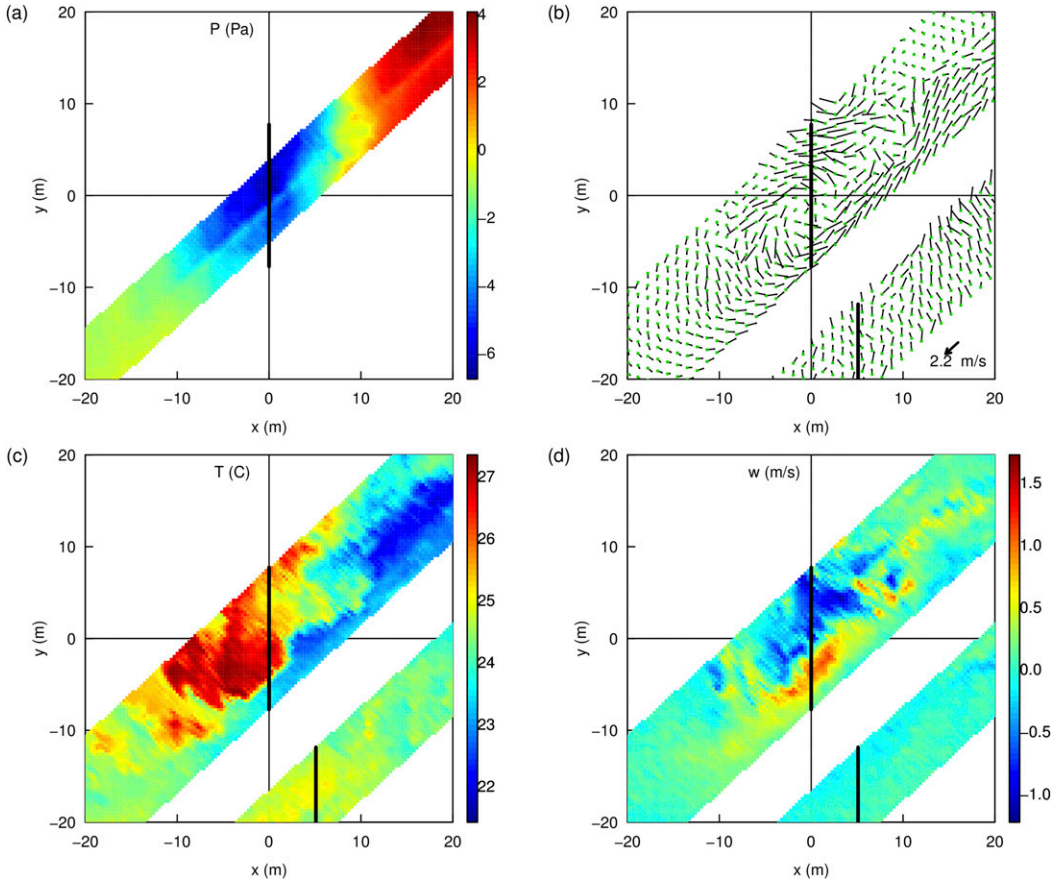

FIG. 13. As in Fig. 3, but for a roll at 0231 PDT 7 Aug 2008. An updraft region is parallel to a downdraft region suggesting mostly horizontal rotation. The stretched-out (in the along-wind direction) horizontal rotation, along with the limited extent of the updraft–downdraft regions, indicates that the roll is tilted at about 11° from the horizontal. The temperature field shows warm air transported downward and cold air transported upward, as expected at night.

associated with flow that changes direction, the majority did not have 360° of rotation (around any axis). However, two classes of events were identified that we can describe.

There are 11 events that clearly represent whirlwinds—7 individual and 2 cases of whirlwind pairs. One example is shown in Fig. 11. This case occurred at 2211 PDT—more than 2 h after local sunset. Note that the updraft in the core region of this whirlwind is cold, as expected in stable conditions at night (where temperature near the ground is colder than the overlying air). With this thermal structure, buoyancy-driven convergence cells as modeled by RF would not be present. Also, although some cases have been reported with dust devils persisting for hours, these dissipated when conditions were no longer ''suitable'' (Ives 1947). Thus, it is quite unlikely that a whirlwind generated in convective conditions would persist for (at least) 2 h into stable conditions. We conclude that another source of convergence must have been the dominant mechanism for the formation of this and (at least) the other night whirlwinds.

Also evident in Fig. 11 is asymmetry in the vertical velocity field, similar to that seen in Fig. 3. Asymmetry is seen in other night whirlwinds as well—for example, the double whirlwind case shown in Fig. 12. We conclude that asymmetry is a characteristic of whirlwinds, independent of their stability environment.

Our second class of night cases is mostly horizontally oriented vortices. Figure 13 shows a roll tilted in the along-wind direction that passed through the bottom rake. There were several such cases, but what is most interesting is that they sometimes were observed in pairs. Figure 14 shows such an example with two parallel, tilted, counterrotating, and along-wind-oriented vortices. A three-dimensional visualization (Fig. 15) of the data from both the top and bottom rakes confirms a tubelike structure for each vortex. The diameter of each vortex is about 2.5 m and length observed is about 10 m,

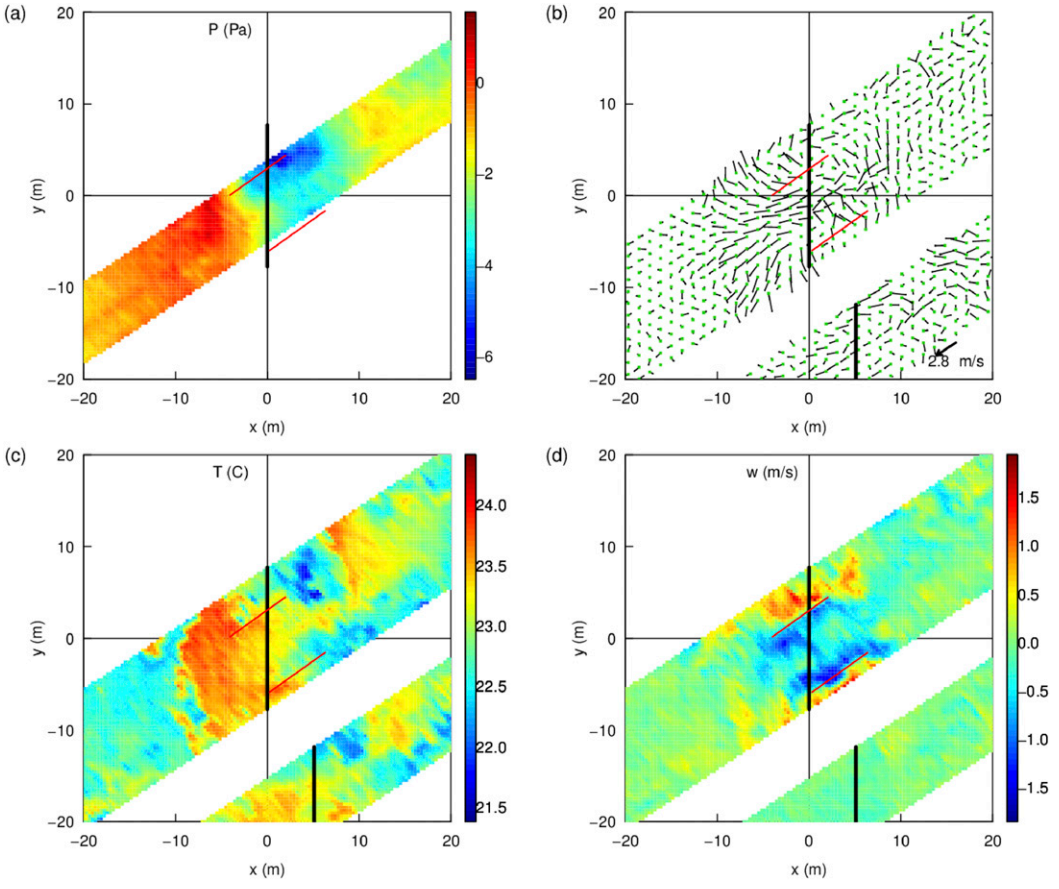

FIG. 14. As in Fig. 13, but for a roll doublet at 0311 PDT 3 Aug 2008. The vertical velocity has updraft–downdraft–downdraft–updraft regions parallel to the mean wind direction, suggesting a pair of horizontal rolls. Red lines are drawn to show their axes of rotation. Their finite extent as sampled by this horizontal cross section suggests that they are tilted. The horizontal velocity shows counterrotation of these two rolls, consistent with the vertical velocity. Also similar to Fig. 13, the temperature field shows a stretched-out region of descending warm air between two ascending regions of cooler air. The pressure field appears to have pressure minima near each roll's axis.

which would imply a tilt angle of approximately 15°. We interpret these to be two legs of a hairpin vortex and thus would be the second study [after Hutchins et al. (2012), using a similar instrument array] to have observed them in atmospheric flows. As described by Adrian (2007), hairpin, or horseshoe, vortices start as spanwise vortex filaments. The middle portion of the filament (the "head") is lifted by a local updraft into higher-velocity fluid that stretches the vortex in the streamwise direction.

After presenting nighttime cases with rotation axes in the vertical and along-wind directions, our final case is a crosswind-oriented nearly horizontal roll (Fig. 16). The axis of rotation was at nearly the height of the bottom rake, so the horizontal flow shows mostly crosswind shear and little rotation. It appears that this roll was about 6 m in diameter and tilted at about 12° from horizontal, as estimated both by how it was sampled by the horizontal array and by its sampling by the vertical rake. This roll does not exhibit the downturning of the edges or horizontal rotation that would be characteristic of the head of a hairpin vortex.

6. Limitations

To transform data from sensor rakes to horizontal cross sections, our analysis necessarily has assumed that the whirlwinds were sampled at one instant in time. Thus, one obvious weakness of our data, for example, is the inability to document the development stages of a single whirlwind.

We were surprised to find a relatively small range of whirlwind sizes. To some extent, the AHATS data are biased by the sizes of the array. However the largest array spanned 48 m and sizes could have been estimated for cases when only part of a whirlwind entered the array. Thus, we should have been able to observe

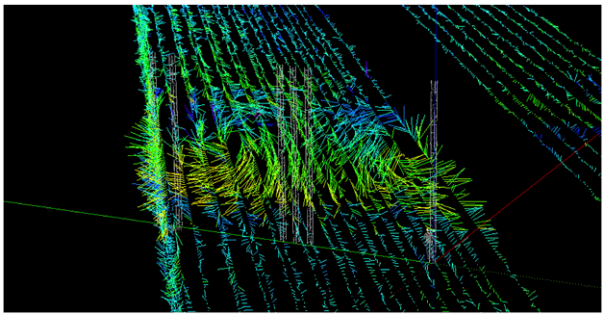

FIG. 15. The roll doublet case shown in Fig. 14 visualized in perspective with every sample from a sonic anemometer displayed as a three-dimensional wind vector color-coded by its temperature. Warm colors (yellow) indicate air temperatures higher than the mean and cool colors (blue) lower than the mean. The six 10-m-high towers supporting the bottom, top, and vertical rakes are shown for scale.

whirlwinds at least 10 times larger than the 8-m median diameter that was found.

This study has not shown any vertical profiles of whirlwinds, despite the extensive discussion of tilt characteristics by several earlier authors. As mentioned above, the AHATS array did have a vertical rake sampling from 0.4 to 8.7 m high. This is not a large height range for whirlwinds, though it could provide some information when a whirlwind passed through. However, our primary detection method relied on the whirlwind passing the pressure sensor in the middle of the bottom rake, which was displaced horizontally by 10–28 m from the vertical rake; thus, it was not possible to sample the vertical structure of the relatively small whirlwinds. Similarly, sodar, radio acoustic sounding system (RASS) sodar, and 915-MHz radar wind profilers were located about 200, 2800, and 4800 m, respectively, from the tower array. Work is ongoing to determine if the RASS sodar observed any of these cases, though temporal averaging in processing the sodar data will smear these events.

7. Conclusions

Vortices that likely were dust devils were sampled during AHATS. It appears that these coherent vortices

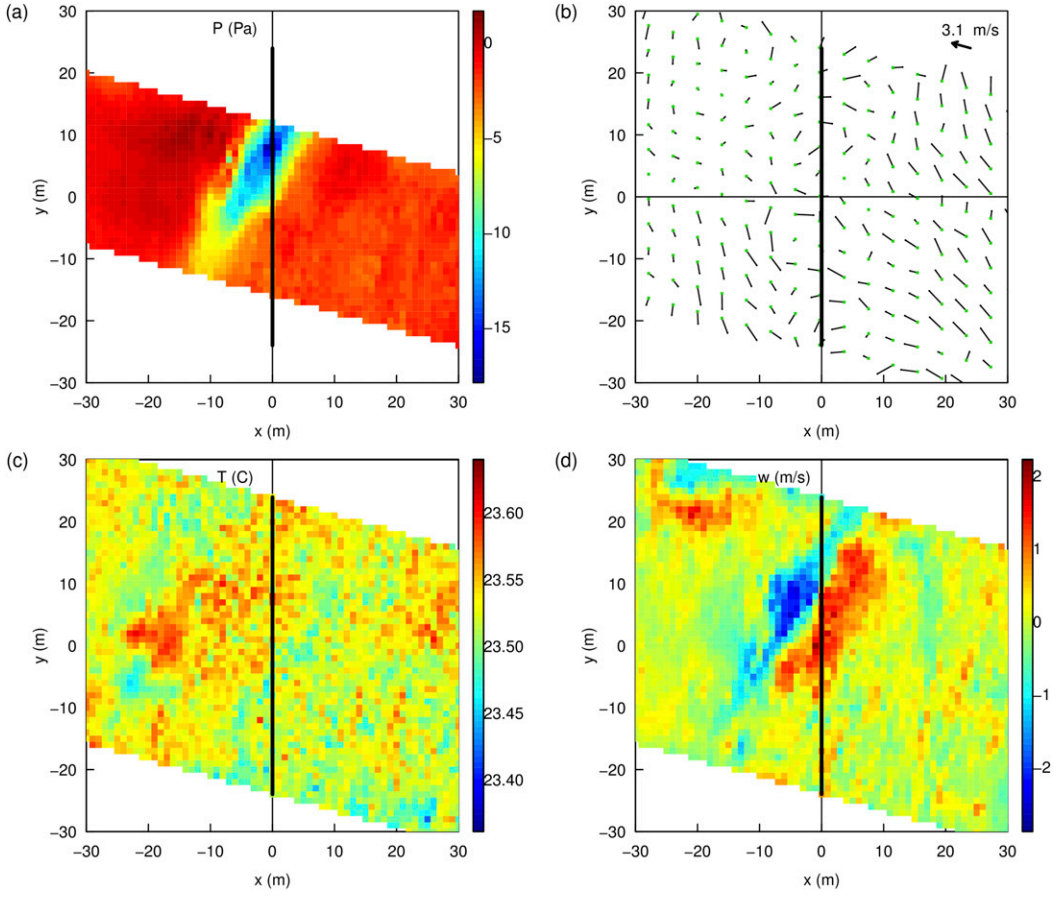

FIG. 16. A slightly tilted crosswind-oriented horizontal roll at 0508 PDT 16 Jul 2008. For this case, measurements were taken at $z = 3.24$ m. Rotation is seen from the updraft–downdraft pair. Little rotation is seen in the horizontal wind field. The temperature field shows a slight amount (on the order of 0.1°C) of cooling in the updraft region.

were quite common, since they were sampled by a sensor array fixed in space. These vortices were never azimuthally symmetric and many had multiple embedded vortices within the region of maximum tangential wind—characteristics that are shared with tornadoes and hurricanes.

However, some cases were encountered that exhibited dust-devil behavior but clearly did not fit the AMS definition. Some cases had values of u_* that probably were not high enough to pick up dust. Whirlwinds were observed in only moderately unstable conditions and even in stable conditions, contrary to the results of Kurgansky et al. (2011). To explain this behavior, we have documented cases of whirlwinds associated with convergence lines and regions of strong horizontal wind shear, supporting recent LES modeling results (Kanak 2005; RF) that whirlwinds are maintained by convergence, though their convergence regions were generated by convection. Like these modeling studies, we cannot comment on how rotation is initiated.

In stable conditions, nonvertically oriented vortices were much more common and were observed in both along- and crosswind orientations. One case of a pair of nearly horizontal counterrotating vortices could be explained as the legs of a hairpin vortex.

All of these structures were easily detected by looking for sharp changes in static pressure—a detection criterion also used by RF. Although fast-response and high-resolution pressure transducers were used for this study, many of the strong whirlwind cases could have been observed by standard barometers with, say, 1-s data reporting and 0.1-mb resolution. We encourage other researchers to examine their data for such events.

Acknowledgments. The first author would like to thank several colleagues for helpful discussion throughout this study: Wen-Chau Lee, Rich Rotunno, Roger Wakimoto, Ned Patton, Tom Horst, Dennis Flannigan (all while at the National Center for Atmospheric Research), and Howie Bluestein (University of Oklahoma). The comments from three anonymous reviewers are also appreciated. We thank the Integrated Surface Flux System staff for supporting a challenging and labor-intensive deployment. The first and second authors were supported by their home institutions. The National Science Foundation funded this experiment and the third author through Awards ATM-0638392 and AGS-1335995.

REFERENCES

Adrian, R. J., 2007: Hairpin vortex organization in wall turbulence. *Phys. Fluids*, **19**, 041301, doi:10.1063/1.2717527.

Arroues, K. D., and J. C. H. Anderson, 1986: Soil survey of Kings County California. Tech. Rep. 1986-479-188/40018, U.S. Government Printing Office, 212 pp. [Available online at http://www.nrcs.usda.gov/Internet/FSE_MANUSCRIPTS/california/CA031/0/kings.pdf.]

Bagnold, R. A., 1954: *The Physics of Blown Sand and Desert Dunes*. Methuen, 265 pp.

Balme, M. R., P. L. Whelley, and R. Greeley, 2003: Mars: Dust devil track survey in Argyre Planitia and Hellas Basin. *J. Geophys. Res.*, **108**, 5086, doi:10.1029/2003JE002096.

Bluestein, H. B., C. C. Weiss, and A. L. Pazmany, 2004: Doppler radar observations of dust devils in Texas. *Mon. Wea. Rev.*, **132**, 209–224, doi:10.1175/1520-0493(2004)132<0209:DROODD>2.0.CO;2.

Carroll, J. J., and J. A. Ryan, 1970: Atmospheric vorticity and dust devil rotation. *J. Geophys. Res.*, **75**, 5179–5184, doi:10.1029/JC075i027p05179.

Danes, R., 1901: *Cassell's History of the Boer War, 1899–1901*. Cassell, 224 pp.

Davies-Jones, R. P., 1986: Tornado dynamics. *Thunderstorm Morphology and Dynamics*, E. Kessler, Ed., Vol. 2, *Thunderstorms: A Social, Scientific, and Technological Documentary*, University of Oklahoma Press, 197–236.

Fitzjarrald, D. E., 1973: A field investigation of dust devils. *J. Appl. Meteor.*, **12**, 808–813, doi:10.1175/1520-0450(1973)012<0808:AFIODD>2.0.CO;2.

Fujita, T., 1955: Results of detailed synoptic studies of squall lines. *Tellus*, **7**, 405–436, doi:10.1111/j.2153-3490.1955.tb01181.x.

Garai, A., E. Pardyjak, G. J. Steenveld, and J. Kleissl, 2013: Surface temperature and surface-layer turbulence in a convective boundary layer. *Bound.-Layer Meteor.*, **148**, 51–72, doi:10.1007/s10546-013-9803-4.

Glickman, T. S., Ed., 2000: *Glossary of Meteorology*. 2nd ed. Amer. Meteor. Soc., 855 pp. [Available online at http://glossary.ametsoc.org/.]

Gu, Z., Y. Zhao, Y. Li, Y. Yu, and X. Feng, 2006: Numerical simulation of dust lifting within dust devils—Simulation of an intense vortex. *J. Atmos. Sci.*, **63**, 2630–2641, doi:10.1175/JAS3748.1.

Horst, T. W., J. Kleissl, D. H. Lenschow, C. Meneveau, C.-H. Moeng, M. B. Parlange, P. P. Sullivan, and J. C. Weil, 2004: HATS: Field observations to obtain spatially filtered turbulence fields from crosswind arrays of sonic anemometers in the atmospheric surface layer. *J. Atmos. Sci.*, **61**, 1566–1581, doi:10.1175/1520-0469(2004)061<1566:HFOTOS>2.0.CO;2.

Hutchins, N., K. Chauhan, I. Marusic, J. Monty, and J. Klewicki, 2012: Towards reconciling the large-scale structure of turbulent boundary layers in the atmosphere and laboratory. *Bound.-Layer Meteor.*, **145**, 273–306, doi:10.1007/s10546-012-9735-4.

Iversen, J. D., R. Greeley, and J. B. Pollack, 1976: Windblown dust on Earth, Mars and Venus. *J. Atmos. Sci.*, **33**, 2425–2429, doi:10.1175/1520-0469(1976)033<2425:WDOEMA>2.0.CO;2.

Ives, R. L., 1947: Behavior of dust devils. *Bull. Amer. Meteor. Soc.*, **28**, 168–174.

Kaimal, J. C., and J. A. Businger, 1970: Case studies of a convective plume and a dust devil. *J. Appl. Meteor.*, **9**, 612–620, doi:10.1175/1520-0450(1970)009<0612:CSOACP>2.0.CO;2.

Kanak, K. M., 2005: Numerical simulations of dust devil–scale vortices. *Quart. J. Roy. Meteor. Soc.*, **131**, 1271–1292, doi:10.1256/qj.03.172.

Kelly, M., J. C. Wyngaard, and P. P. Sullivan, 2009: Application of a subfilter-scale flux model over the ocean using OHATS field data. *J. Atmos. Sci.*, **66**, 3217–3235, doi:10.1175/2009JAS2903.1.

Kepert, J., and Y. Wang, 2001: The dynamics of boundary layer jets within the tropical cyclone core. Part II: Nonlinear

enhancement. *J. Atmos. Sci.*, **58**, 2485–2501, doi:10.1175/1520-0469(2001)058<2485:TDOBLJ>2.0.CO;2.

Koch, J., and N. O. Renno, 2005: The role of convective plumes and vortices on the global aerosol budget. *Geophys. Res. Lett.*, **32**, L18806, doi:10.1029/2005GL023420.

Kurgansky, M. V., A. Montecinos, V. Villagran, and S. M. Metzger, 2011: Micrometeorological conditions for dust-devil occurrence in the Atacama Desert. *Bound.-Layer Meteor.*, **138**, 285–298, doi:10.1007/s10546-010-9549-1.

Lee, W.-C., and J. Wurman, 2005: Diagnosed three-dimensional axisymmetric structure of the Mulhall tornado on 3 May 1999. *J. Atmos. Sci.*, **62**, 2373–2393, doi:10.1175/JAS3489.1.

Mueller, C. K., and R. E. Carbone, 1987: Dynamics of a thunderstorm outflow. *J. Atmos. Sci.*, **44**, 1879–1898, doi:10.1175/1520-0469(1987)044<1879:DOATO>2.0.CO;2.

Nguyen, K. X., T. W. Horst, S. P. Oncley, and C. Tong, 2013: Measurements of the budgets of the subgrid-scale stress and temperature flux in a convective atmospheric surface layer. *J. Fluid Mech.*, **729**, 388–422, doi:10.1017/jfm.2013.302.

Patton, E. G., and Coauthors, 2011: The Canopy Horizontal Array Turbulence Study. *Bull. Amer. Meteor. Soc.*, **92**, 593–611, doi:10.1175/2010BAMS2614.1.

Raasch, S., and T. Franke, 2011: Structure and formation of dust devil–like vortices in the atmospheric boundary layer: A high-resolution numerical study. *J. Geophys. Res.*, **116**, D16120, doi:10.1029/2011JD016010.

Shea, D. J., and W. M. Gray, 1973: The hurricane's inner core region. I. Symmetric and asymmetric structure. *J. Atmos. Sci.*, **30**, 1544–1564, doi:10.1175/1520-0469(1973)030<1544:THICRI>2.0.CO;2.

Sinclair, P. C., 1964: Some preliminary dust devil measurements. *Mon. Wea. Rev.*, **92**, 363–367, doi:10.1175/1520-0493(1964)092<0363:SPDDM>2.3.CO;2.

——, 1969: General characteristics of dust devils. *J. Appl. Meteor.*, **8**, 32–45, doi:10.1175/1520-0450(1969)008<0032:GCODD>2.0.CO;2.

Smith, R. K., and L. M. Leslie, 1976: Thermally driven vortices: A numerical study with application to dust-devil dynamics. *Quart. J. Roy. Meteor. Soc.*, **102**, 791–804, doi:10.1002/qj.49710243409.

Taylor, G. I., 1938: The spectrum of turbulence. *Proc. Roy. Soc. London*, **164A**, 476, doi:10.1098/rspa.1938.0032.

Tong, C., J. C. Wyngaard, S. Khanna, and J. G. Brasseur, 1998: Resolvable- and subgrid-scale measurement in the atmospheric surface layer: Technique and issues. *J. Atmos. Sci.*, **55**, 3114–3126, doi:10.1175/1520-0469(1998)055<3114:RASSMI>2.0.CO;2.

Tratt, D. M., M. H. Hecht, D. C. Catling, E. C. Samulon, and P. H. Smith, 2003: In situ measurement of dust devil dynamics: Toward a strategy for Mars. *J. Geophys. Res.*, **108**, 5116, doi:10.1029/2003JE002161.

Wilczak, J. M., and J. E. Tillman, 1980: The three-dimensional structure of convection in the atmospheric surface layer. *J. Atmos. Sci.*, **37**, 2424–2443, doi:10.1175/1520-0469(1980)037<2424:TTDSOC>2.0.CO;2.

Willis, G. E., and J. W. Deardorff, 1979: Laboratory observation of turbulent penetrative-convection planforms. *J. Geophys. Res.*, **84**, 295–302, doi:10.1029/JC084iC01p00295.

Wurman, J., 2002: The multiple-vortex structure of a tornado. *Wea. Forecasting*, **17**, 473–505, doi:10.1175/1520-0434(2002)017<0473:TMVSOA>2.0.CO;2.